

Full Length Article

BiOBr microspheres anchored with Cu₂O nanoparticles and rGO: A Z-scheme heterojunction photocatalyst for efficient reduction of Cr(VI) under visible light irradiation

Jian Ma^a, Congjie Liang^a, Changjiang Yu^a, Huaming Li^b, Hui Xu^b, Yingjie Hua^{a,*}, Chongtai Wang^{a,*}

^a School of Chemistry and Chemical Engineering of Hainan Normal University, Key Laboratory of Electrochemical Energy Storage and Energy Conversion of Hainan Province, Key Laboratory of Electrochemical Energy Storage and Light Energy Conversion Materials of Haikou City, Haikou 571158, PR China

^b Institute for Energy Research, School of the Environment and Safety Engineering, Jiangsu University, Zhenjiang 212013, PR China

ARTICLE INFO

Keywords:

Cu₂O/rGO/BiOBr
Z-scheme heterojunction
Synergy effect
Photocatalysis
Cr(VI) reduction

ABSTRACT

Photocatalytic reduction of hexavalent chromium (Cr(VI)) is an effective way to reduce its environmental risk. However, it remains a challenge to achieve a high removal rate in mild conditions. In order to efficiently remove Cr(VI) from water, a novel Z-scheme heterojunction composite photocatalyst rCB-20 (Cu₂O/rGO/BiOBr, 20% Cu₂O) was successfully prepared using a simple two-step strategy in this work. The characterizations of the catalyst show that the Z-scheme heterojunction formed between Cu₂O and BiOBr is favorable for facilitating the separation of photogenerated carriers. The existence of rGO can reduce the resistance of electron transport. Therefore, the composite photocatalyst exhibits a very high photocatalytic activity in the photoreduction of Cr(VI). For example, using it to completely remove Cr(VI) with a concentration of 20 mg•L⁻¹ in the pH = 4 solution only requires 40 min. Even the complete removal of the same concentration of Cr(VI) in neutral water at pH 7 does not take more than 90 min. Meanwhile, it possesses a high stability in catalytic activity and structure.

1. Introduction

With the development of industrialization, water resources have been polluted by various heavy metal ions to different degrees. Among them, hexavalent chromium, Cr(VI), is a common contaminant in wastewater [1,2]. Its releasing into drinking water will lead to some serious diseases to humans, e.g. cancer, thus threat to human health [3,4]. Therefore, it is urgent to develop feasible technologies for eliminating Cr(VI) from water. Fortunately, some methods to remove Cr(VI) such as adsorption [5–8], precipitation [9], chemical reduction [10], and photocatalysis have been developed [11–14]. But the adsorption method cannot remove Cr(VI) thoroughly, the precipitation method has the problem of secondary treatment, and the chemical reduction method needs a harsh acidic condition. Only the photocatalysis is considered to be the most promising method [15–17]. It not only avoids the shortcomings of the above methods, but also has a low cost due to the simple process and the use of priceless sunlight. Moreover, it is more suitable for handling amounts of water. However, this technology requires photocatalysts with semiconducting properties because the conversion

of light energy depends on the transition of electrons in the valence band to conduction band upon light irradiation. The width of the band gap between the valence band and conduction band determines the wavelength of light absorbed by the catalyst. In general, the photoelectrons generated by photoexcitation readily recombine with the corresponding holes, resulting in a low photocatalytic efficiency. Therefore, separation of photoelectrons and holes plays a crucial role for enhancing photocatalytic efficiency and deeply influenced by the band gap structure [18,19]. It is well known that doping other element in intrinsic semiconductor or compositing two or more semiconductor materials can change the band gap structure of the photocatalyst, thus is beneficial to promote the separation of photogenerated electrons and holes. Transition metal oxides are often used to construct composite photocatalysts due to their easy preparation and morphology control. Cu₂O, as one of the transition metal oxides, has been found to be an ideal candidate for the photoreduction of Cr(VI) due to its low cost, visible light response and suitable CB potential [20,21]. But the Cu (I) of Cu₂O suffers readily from oxidation under light irradiation due to the photogenerated holes not compensated by electrons [22–24], leading to a so called

* Corresponding authors.

E-mail addresses: 521000hua282@sina.com (Y. Hua), oehy2014@163.com (C. Wang).

<https://doi.org/10.1016/j.apsusc.2022.155247>

Received 31 August 2022; Received in revised form 3 October 2022; Accepted 7 October 2022

Available online 12 October 2022

0169-4332/© 2022 Elsevier B.V. All rights reserved.

photocorrosion. To overcome this issue, some strategies such as addition of sacrificial agents [25], construction of nanostructures [26–28], and coupling with nonmetallic semiconductors [29–31] have been adopted. Researches show that coupling with nonmetallic semiconductors is an effective way to inhibit the photocorrosion of Cu_2O owing to the formation of a Z-scheme heterojunction [32–35]. In addition, the formation of Z-scheme heterojunction can also improve the redox capacity of the photocatalyst.

In order to construct a Z-scheme heterojunction using Cu_2O as one of the composite photocatalytic materials, it is required to choose another semiconductive material that has a matched band gap structure with that of Cu_2O . Recently, BiOX ($X = \text{Cl}, \text{Br}, \text{I}$) has attracted attention on account of its layered structure and band gap structure [36–40]. For example, the internal electric field between the $[\text{Bi}_2\text{O}_2]^{2+}$ layer and the X^- layer in the lattice is beneficial to the effective separation of the photogenerated electron–hole pairs [36–40]. BiOBr is one of the BiOX compounds that is widely used in photoreduction of Cr(VI) [41,42]. Specifically, the conduction band (CB) edge of BiOBr lies between the CB and valence band (VB) potentials of Cu_2O [43–45], thus providing a possibility to form Z-scheme heterojunction when BiOBr and Cu_2O are composited. In addition, electron mediator in heterojunction composites is also indispensable [46–49] because it acts as a role of collecting and transferring photogenerated electrons. The electron mediators often used include ion and solid-state type ones. The solid-state electron mediators are considered to possess the advantages of high electron transfer efficiency and mild reaction conditions. Among them, reduced graphene oxide (rGO) maybe prevails over the most commonly used noble metals because of its high transparency, more adsorption sites and conjugated π structure that can increase the interaction between rGO and semiconductors [50]. Recently, some studies have shown that rGO is truly an ideal electron mediator in improving the photocatalytic activity of semiconductors [51,52].

Based on the above understanding and reasons, a series of $\text{Cu}_2\text{O}/\text{rGO}/\text{BiOBr}$ composites were prepared using a two-step strategy in this work, and the structure, morphology, photocatalytic performance and reaction mechanism etc of the prepared materials were studied in detail. The results show that the $\text{Cu}_2\text{O}/\text{rGO}/\text{BiOBr}$ composite presents an excellent photocatalytic performance to reduce Cr(VI) under visible light irradiation, and the photocorrosion of Cu_2O is restrained due to the formation of Z-scheme heterojunction.

2. Experimental

2.1. Preparation of photocatalysts

All of the reagents used for synthesis were purchased from Aladdin Reagent Co., Ltd, and were of analytical grade and used as received without additional purification.

2.1.1. Preparation of BiOBr

1 mmol of KBr and a certain amount of PVP were dissolved into 20 mL of deionized water in beaker A, and the solution was stirred for 45 min to make them uniformly dispersed. In addition, 1 mmol of $\text{Bi(NO}_3)_3$ and 20 mL of deionized water were added into beaker B, and then sonicated for 15 min. The solution in beaker A was added into beaker B, and the pH of the mixed solution was adjusted to 6 using NaOH ($1 \text{ mol}\cdot\text{L}^{-1}$). Subsequently, the solution was transferred to a 60 mL Teflon autoclave and maintained at 100°C for 1 h. After cooling to room temperature, the product was collected, and washed several times with deionized water and ethyl alcohol, respectively, and dried at 40°C for 12 h.

2.1.2. Preparation of $\text{Cu}_2\text{O}/\text{rGO}/\text{BiOBr}$ composite

A certain amount (e.g. 381 mg, 166 mg, and 94 mg) of BiOBr and 6 mg of rGO were dispersed in 50 mL of deionized water, and sonicated for 30 min to obtain a homogeneous mixed solution. Subsequently, 60 mg of

$\text{Cu(AC)}_2\cdot\text{H}_2\text{O}$, 0.1 g of CTAB and 0.1 g of EDTA were dissolved in the above mixed solution, and then dropwise adding 20 mL of NaOH ($0.45 \text{ mol}\cdot\text{L}^{-1}$) and 20 mL of ascorbic acid ($0.3 \text{ mol}\cdot\text{L}^{-1}$). The as-resulted mixed solution was stirred for 30 min, and the produced precipitate was separated by centrifugation, and then washed with deionized water and ethanol three times, respectively, and dried at 60°C in vacuum for 10 h to obtain the target products. The mass ratios of Cu_2O in the composites were 10%, 20%, and 30%, respectively. The composite samples were labeled as rCB-x, where x is the mass ratio of Cu_2O . For comparison, pure Cu_2O was prepared without adding BiOBr under the same conditions. In addition, the BiOBr/rGO , $\text{rGO}/\text{Cu}_2\text{O}$, and $\text{BiOBr}/\text{Cu}_2\text{O}$ samples were also synthesized according to the similar procedures.

2.2. Characterization of photocatalysts

The crystal structure of samples were characterized using X-ray diffraction (XRD); $\text{Cu-K}\alpha$ as the radiation source, 40 kV tube voltage and 140 mA current (Ultimalv type, Bruker, Germany). The Raman spectra were recorded using a Raman spectrometer (XPLORE plus, Horiba-JY, France) at a laser excitation wavelength of 532 nm. The FT-IR spectra of the samples were recorded using a Nicolet 6700 infrared spectrometer (Thermo scientific, USA); KBr pellet. The surface morphology and internal microstructure as well as the element composition of samples were characterized using a thermal field emission scanning electron microscope (SEM, JSM-7100F, JEOL, Japan) and a transmission electron microscope with an X-ray energy dispersive spectroscope (EDS) (TEM, Tecnai G2F20, Holland), respectively. The UV–visible diffuse reflectance spectroscopy (DRS) of samples was measured using an ultraviolet–visible spectrophotometer (T10, Beijing General Instrument Co., Ltd., China). The element composition of samples and valence state were analyzed by using X-ray photoelectron spectroscopy (XPS, K-alpha, thermo, Germany). The specific surface area and total pore volume of samples were measured using a N_2 adsorption/desorption equipment (BET, Kubo X1000, China). The photoluminescence (PL) spectra were recorded using a Fluorolog-3 photoluminescence spectrometer (Horiba, Fluorolog-3, USA). The surface potentials of samples under dark and light irradiation ($\lambda > 400 \text{ nm}$) conditions were measured using the Kelvin probe force microscope (KPFM) equipped in a scanning probe microscope (SPM) system (Bruker Dimension icon, Germany).

2.3. Photocatalytic reduction of Cr(VI)

The reaction of photocatalytic reduction of Cr(VI) was carried out in a quartz reactor. Typically, 20 mg of photocatalyst was added into 50 mL of $20 \text{ mg}\cdot\text{L}^{-1} \text{K}_2\text{Cr}_2\text{O}_7$ solution, and then stirred in dark for 50 min to get an adsorption–desorption balance. After that, the reaction of photocatalytic reduction of Cr(VI) was conducted using a 300 W Xenon lamp (HSX-F300, NBet, China) equipped with a cutoff filter ($\lambda \geq 420 \text{ nm}$) as the light source. During reaction, 1.2 mL of solution was taken out at regular intervals using the needle tube and filtered. Accurately taking 1 mL of filtrate and putting it into a small glass bottle, and then 9 mL of $0.2 \text{ mol}\cdot\text{L}^{-1} \text{H}_2\text{SO}_4$ and 200 μL of $500 \text{ mg}\cdot\text{L}^{-1}$ diphenylcarbazide were added into the filtrate to perform a chromogenic reaction. After the color of the solution was stable for 8 min, the absorbance of solution was determined using a UV–vis spectrophotometer. The concentration of total chromium was measured using an inductively coupled plasma–optical emission spectrometer (ICP-OES, 7000 series).

2.4. Electrochemical measurements

The Electrochemical impedance spectroscopy (EIS) of samples were measured in a standard three-electrode configuration using an electrochemical station (CHI 660e, Chenhua, China). Samples deposited on the $1.0 \text{ cm} \times 1.0 \text{ cm}$ FTO glass were used as the working electrode. A Pt wire and a saturated calomel electrode (SCE) as the counter electrode and reference one, respectively. The supporting electrolyte was the 0.1 M

Na₂SO₄ solution. The frequency used in EIS measurements was from 100 kHz to 0.1 Hz.

3. Results and discussion

3.1. Characterization of photocatalysts

3.1.1. XRD characterization

Fig. 1a shows the XRD patterns of the samples. It can be seen that all of the diffraction peaks of BiOBr and Cu₂O samples were consistent with those assigned to the pure BiOBr and Cu₂O crystals (JCPDS NO. 09-0393 and JCPDS NO. 05-0667), suggesting that BiOBr and Cu₂O with pure crystalline phase have successfully been prepared. Moreover, the BiOBr is attributed to a tetragonal crystalline phase [4], and the Cu₂O to a cubic crystalline phase [20]. In particular, the characteristic diffraction peaks of BiOBr were still detected in the composite materials, indicating that after compositing with Cu₂O and rGO, the crystalline phase structure of BiOBr does not change. At the same time, the diffraction peak intensity of BiOBr decreases gradually with increasing the dosage of Cu₂O, which results from the declined crystallinity owing to the influence of Cu₂O that highly disperses on the BiOBr surface [53,54]. High crystallinity of sample indicates less concentration of defect, which is related to the recombination rate of photocarriers [54]. Hence, the crystallinity of sample may be a contributing factor that influences the photocatalytic activity, and it will be discussed later. Moreover, the diffraction signals of Cu₂O and rGO in the composite samples were not observed, which may be related to their high dispersion and low crystallinity.

3.1.2. Raman and IR characterizations

The Raman spectra of the BiOBr, Cu₂O, rGO, and rCB-20 samples are illustrated in Fig. 1b. There are two peaks observed obviously for the pure rGO sample. The peak emerging at approximately 1317 cm⁻¹ is defined as D peak, which is a defect peak due to inter-valley scattering. The peak at 1559 cm⁻¹ is called to be G peak, which corresponds to the sp²-hybridized carbon [50]. For the pure BiOBr, there is a peak appearing at 91 cm⁻¹, which is ascribed to the A_{1g} internal Bi-Br stretching mode [55]. As for the pure Cu₂O, the feature peak occurs at 258 cm⁻¹ due to the 2Γ₁₅ vibration mode [56]. These feature peaks of BiOBr, Cu₂O, and rGO are all detected in the rCB-20 sample, indicating that the desired composite has successfully been prepared.

In addition to Raman spectroscopy, FTIR was further employed to characterize the chemical structures of the prepared samples. The results are shown in Fig. S1 (in Supporting information). For all of the samples, an absorption band near 3439 cm⁻¹ can be observed. This is ascribed to the -OH stretching vibrations from adsorbed H₂O molecules [41]. The

absorption peaks at 1666 cm⁻¹ and 1430 cm⁻¹ are assigned to the Br-Br symmetric and asymmetric stretching vibrations in BiOBr, respectively [7]. The absorption peak near 533 cm⁻¹ was attributed to the vibration of Bi-O bond [7,41]. A sharp absorption peak at about 630 cm⁻¹ was assigned to the Cu-O vibration in Cu₂O [57]. The absorption bands at 1642 cm⁻¹ and 1549 cm⁻¹ result from the C=C and C-C bending vibrations in rGO, respectively [57]. As shown in Fig. S1b, both the characteristic peaks of BiOBr (around 1668 cm⁻¹ and 537 cm⁻¹) and the vibration peak of Cu₂O (around 630 cm⁻¹) are all observed in the rCB-x composites; however, the weak peak of Br-Br asymmetric stretching vibration is almost not observed in the rCB-20 and rCB-30 samples due to the decline of BiOBr content. Moreover, the skeletal vibrations of rGO are overlapped with the characteristic absorption bands of BiOBr.

3.1.3. SEM and TEM characterizations

To reveal the surface morphology and internal microstructure of the prepared samples, SEM and TEM characterizations were performed. The results are illustrated in Fig. 2. It can be seen from Fig. 2a that the BiOBr presents a morphology of hierarchical microspheres with the diameter of 500 nm–1 μm. Whereas the Cu₂O sample consists of a large number of particles aggregated together (Fig. 2b), and the size of these particles is approximately 80–100 nm. As for the rCB-20 sample, it can be observed that the BiOBr microspheres are covered by the grown Cu₂O particles and rGO fragments (Fig. 2c), which leads to a mastoid rough surface of BiOBr microspheres. Furthermore, it can be seen from Fig. S2 that the coverage of the BiOBr microsphere surface is gradually increased with increasing the Cu₂O dosage. The morphology of composite still remains the spherical feature of pristine BiOBr, and the particle size haven't changed much. It can be expected that the mastoid rough surface of the composite will be favorable for the light absorption, just like the surface of green plant leaves. In addition, the Cu₂O particles in rCB-30 showed series agglomeration, which may affect the rates of electron transport. The TEM images in Fig. 2 d-f reveal the internal microstructure of samples. It can be seen that the inside of the synthesized composite microspheres is a farctate structure composed of many BiOBr crystals. The lattice fringes of these crystals can be clearly observed, e.g. those lattice fringes with a lattice spacing of 0.28 nm, which correspond to the (102) crystal plane of BiOBr crystal [55]. Whereas the Cu₂O nano particles disperse on the surface of the BiOBr microspheres and expose those lattice fringes with a lattice spacing of 0.24 nm, which correspond to the (111) plane of cubic Cu₂O [20]. The rGO lies between Cu₂O and BiOBr, but its lattice fringes are not observed due to its low crystallinity (Fig. 2e). The EDS mapping images from TEM in Fig. 2f indicates the elemental distribution of rCB-20 with Bi, Br, O, Cu and C (as shown in Fig. 2g). Therefore, SEM and TEM characterizations demonstrate the prepared target composite to be composed of many

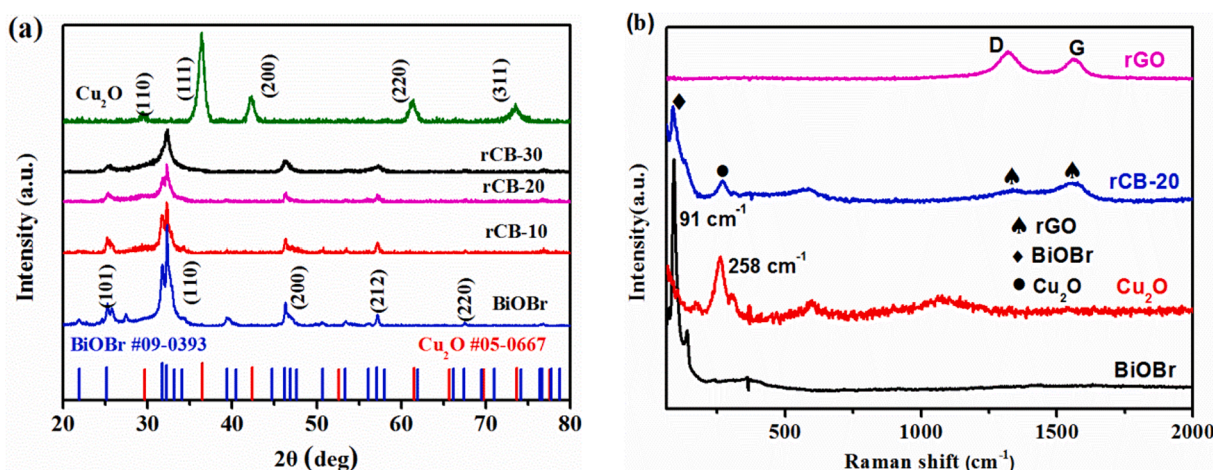


Fig. 1. (a) XRD patterns of the samples. (b) Raman spectra of BiOBr, rGO, Cu₂O, and rCB-20.

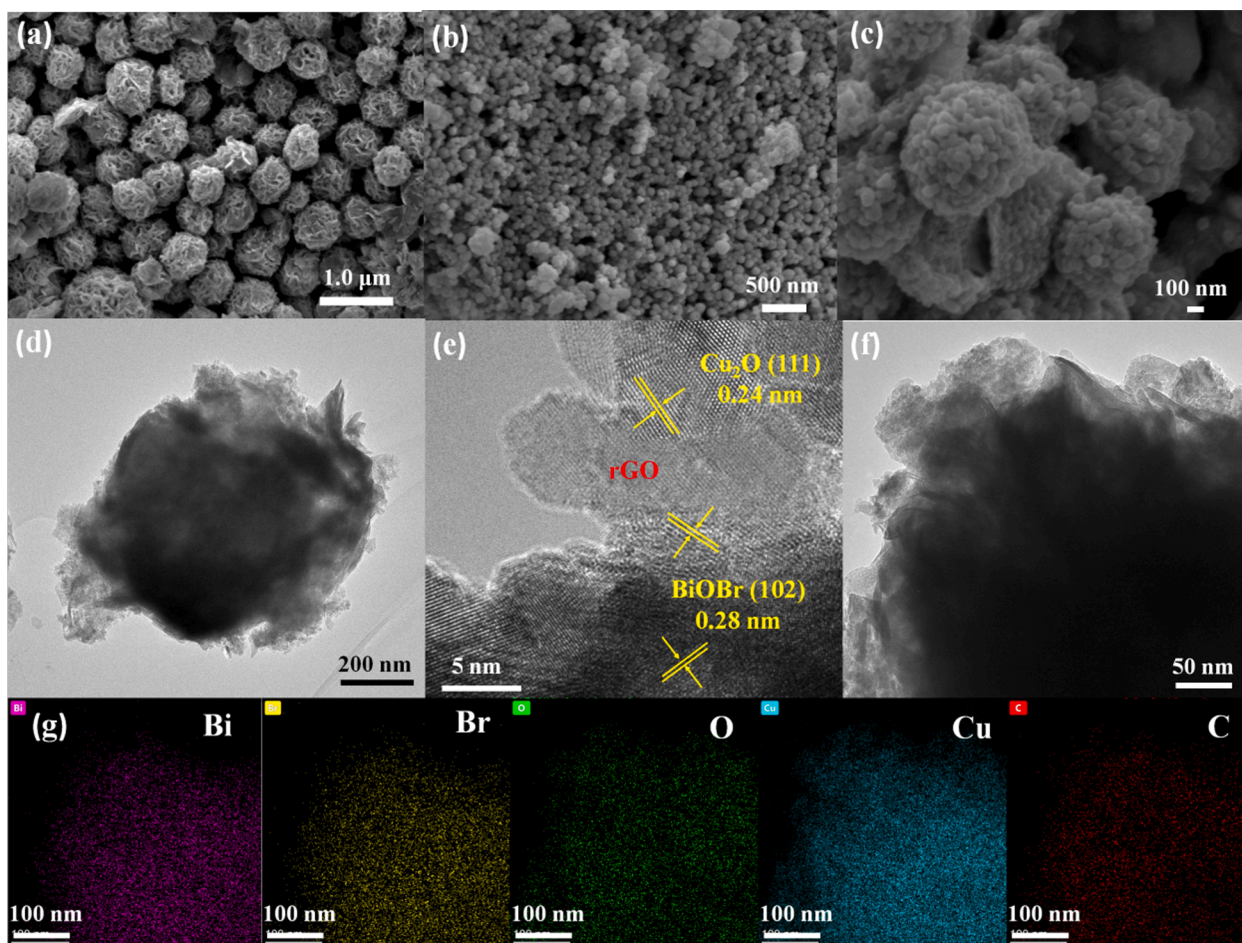


Fig. 2. SEM images of the synthesized samples: (a) BiOBr, (b) Cu_2O , (c) rCB-20. (d)–(f) TEM images of rCB-20. (g) EDS mapping of rCB-20.

microspheres with a mastoid rough surface morphology and the $\text{Cu}_2\text{O}/\text{rGO}/\text{BiOBr}$ microstructure.

3.1.4. Band gap structure characterization

In order to understand the light absorption properties and band gap structure of the prepared samples, measurements of their UV–vis absorption spectra were performed on an ultraviolet–visible spectrophotometer. The results are shown in Fig. 3. It can be seen that the absorption edge of the BiOBr sample is at approximately 430 nm. The

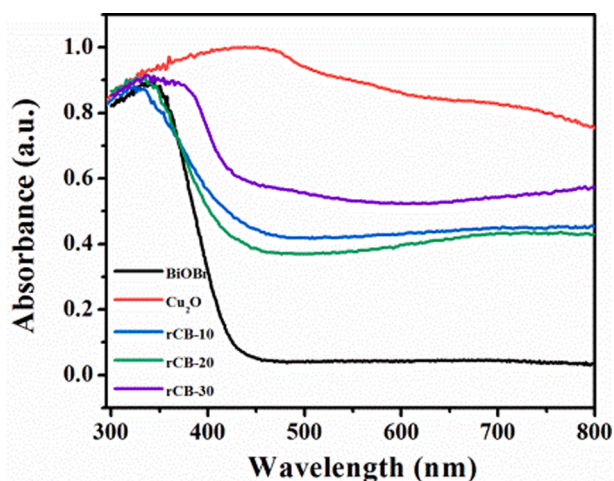


Fig. 3. UV–vis absorption spectra of the prepared samples.

Cu_2O sample has a continuous absorption in both the UV and visible light region, and the maximum absorption is at around 475 nm. The wide light absorption range of the Cu_2O sample maybe associates with its small particle size [20]. In addition to a gradual redshift of the absorption edge, the absorption intensity of the rCB composite samples increases with the increase of Cu_2O content. This is attributed to the contribution of Cu_2O in the composite. According to the Tauc equation, the band gap of the BiOBr and Cu_2O is estimated to be 2.7 and 1.9 eV, respectively. (see Fig. S3a and S3b in Supporting information), consistent with the previous reports [58,59].

The energy level of the valence band (VB) top position of Cu_2O and BiOBr can be determined by measuring the valence band X-ray photoelectron spectrum (VBXPS). As shown in Fig. 4a, the energy levels of the valence band top of Cu_2O and BiOBr are estimated to be 0.5 and 2.0 eV, respectively, by making a tangent line at the Intensity–Binding energy curves. Hence, the energy levels of the conduction band (CB) bottom of Cu_2O and BiOBr are calculated to be -1.4 and -0.7 eV, respectively, according to the VB energy level and band gap values yielded above. On the basis of these results, a schematic diagram to describe the band gap structure of Cu_2O and BiOBr is presented in Fig. 4b. It can be seen that when the Cu_2O and BiOBr are used to construct a Z-scheme heterojunction for photocatalysis, their band gap structures are matched.

3.1.5. XPS characterization

XPS was further used to characterize the chemical elements and their valence state in the prepared samples. As shown in Fig. 5a, the two peaks of Br 3d at ~ 68 and ~ 67 eV in the high resolution spectra are associated with the Br $3d_{3/2}$ and Br $3d_{5/2}$ of Br^- , respectively [60]. The O 1s spectra of BiOBr, Cu_2O , and rCB-20 samples are fitted to two peaks (Fig. 5b). The

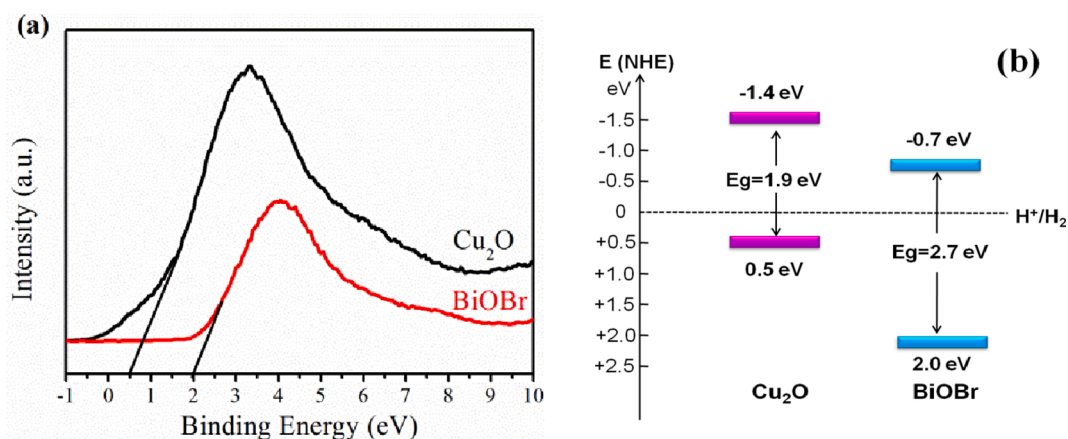


Fig. 4. (a) Valence band X-ray photoelectron spectra of Cu_2O and BiOBr . (b) Schematic diagram describing the band structures of Cu_2O and BiOBr .

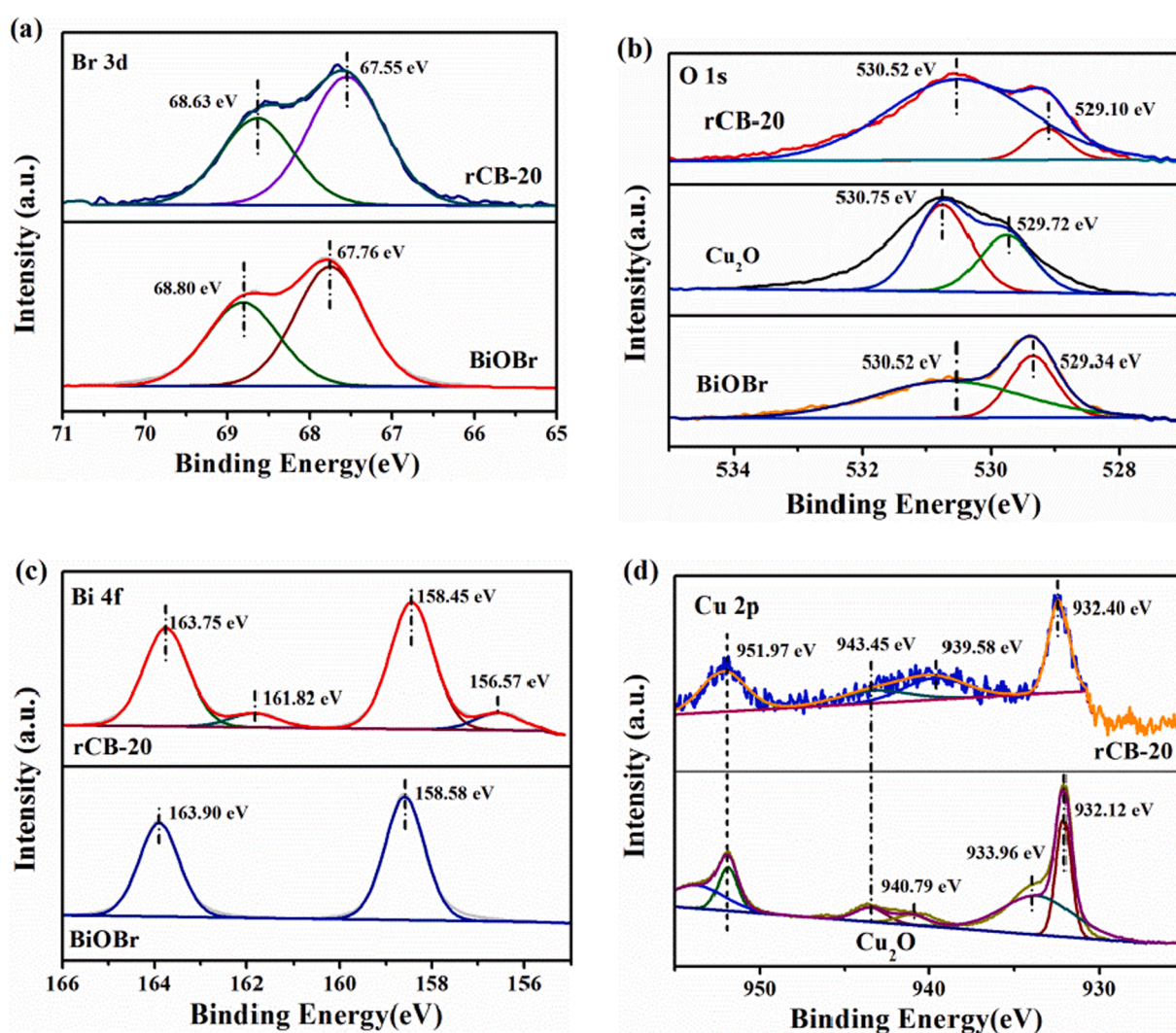


Fig. 5. High-resolution XPS spectra of (a) Br 3d, (b) O 1s, (c) Bi 4f, and (d) Cu 2p of the samples.

peak at ~ 529 eV is assigned to the lattice oxygen in BiOBr or Cu_2O , and the peak at ~ 530.5 eV corresponds to the oxygen of surface hydroxyl groups (O–H bonding) [44,61,62]. The peak positions of O 1s in the rCB-20 sample almost remain unchanged compared to those of the pristine BiOBr . Fig. 5c shows the Bi 4f spectra of the BiOBr and rCB-20 samples. The two peaks at ~ 164 and ~ 158 eV are assigned to the Bi $4f_{5/2}$ and Bi

$4f_{7/2}$ of Bi^{3+} , respectively [63–65]. It is worth noting that there are two weak peaks appearing at 161.82 and 156.57 eV for the rCB-20 sample, which are assigned to the metallic Bi [66]. Existence of Bi^0 is due to the reduction of a small portion of Bi^{3+} in the rCB preparation process. Fig. 5d shows the Cu 2p spectra of the Cu_2O and rCB-20 samples. The two main peaks at ~ 932 and ~ 952 eV are assigned to the Cu $2p_{3/2}$ and

Cu 2p_{1/2} of Cu⁺ [67,68]. The additional peaks at ~943, ~940, and ~933 eV are assigned to the higher valence state of Cu [67,68], indicating that a small portion of Cu⁺ can be oxidized under natural light irradiation.

When comparing the high resolution spectra in Fig. 5, it can be found that the peak positions of Br 3d and Bi 4f in the rCB-20 sample shift a little to the direction of lower binding energy compared to those in the pristine BiOBr. Whereas the peak corresponding to Cu 2p_{3/2} shifts to the direction of higher binding energy. According to these phenomena and previous reports [32,69], it can be deduced that electron migration from Cu₂O to BiOBr occurs in the rCB-20 composite. On the basis of the aforementioned analysis regarding the band gap structures of Cu₂O and BiOBr, this is easy to understand because the Fermi level of electrons in Cu₂O is higher than that in BiOBr. In other words, when these two semiconductors come into contact with each other, meeting the thermodynamic requirement of Fermi level equilibrium makes electrons spontaneous transfer from Cu₂O to BiOBr, thus leading to the formation of a self-built electric field (*E*) at the interface inside the composite materials. The direction of the electric field is from Cu₂O to BiOBr. Existence of a self-built electric field provides an essential precondition for the formation of Z-scheme heterojunction.

3.1.6. Specific surface area

The specific surface area is an important parameter for a photocatalyst because the photocatalytic reaction takes place on the surface. In order to get the data concerning the specific surface area of the BiOBr and rCB-20 samples, their N₂ adsorption-desorption isotherms were measured using a N₂ adsorption/desorption equipment. The results are shown in Fig. 6a. It can be seen that the N₂ adsorption-desorption isotherms of the BiOBr and rCB-20 samples present type IV with an H3 hysteresis loop in the range of 0.4–1.0 *p/p*₀, confirming the existence of mesopores. On the basis of the N₂ adsorption-desorption isotherms, the specific surface areas of the BiOBr and rCB-20 samples were estimated to be 10.06 and 8.81 m²•g⁻¹, respectively (see Table S1 in Supporting information). It should be noted that the specific surface area of the rCB-20 composite has an obvious decline compared to the pristine BiOBr. This is because the morphology and pore size distribution of the rCB-20 composite varied after BiOBr was incorporated with rGO and Cu₂O (Fig. 2c and Fig. 6b). The pore size distribution of the BiOBr sample mainly focus on around 30 and 128 nm, whereas the rCB-20 sample mainly on around 60 and 160 nm. The corresponding pore volumes are 0.1275 cm³•g⁻¹ and 0.1321 cm³•g⁻¹, respectively.

3.2. Photocatalytic performance

In order to evaluate the photocatalytic performance of the prepared samples, the reduction of Cr(VI) under visible light irradiation was used as a probe to carry out a series of photocatalytic experiments. Prior to the photocatalytic reduction of Cr(VI), the adsorption reaction of catalyst towards Cr(VI) was carried out first. As shown in Fig. 7a, an adsorption equilibrium was reached when the reaction suspension was stirred in the dark for 50 min. Moreover, the rCB composite catalysts exhibited better adsorption capacity towards Cr(VI) than the pristine Cu₂O and BiOBr. After starting the photocatalytic reaction, the rCB-20 composite catalyst showed the best photocatalytic activity in the reduction of Cr(VI) among all of the prepared samples, e.g. completely reducing the Cr(VI) with a concentration of 20 mg•L⁻¹ in the pH = 4 solution only needs 40 min, much faster than the pristine Cu₂O or BiOBr (Fig. 7a and b). It should be noted that the Cu₂O content has an obvious influence on the photocatalytic activity of the composite catalysts in the reduction of Cr(VI). The variations of the removal efficiencies for Cr(VI) by the composite samples could be due to the following reasons: first, efficient photogenerated carriers' transfer and separation cannot occur when the Cu₂O content is insufficient (<20%); second, as illustrated in the SEM results, the Cu₂O particles in rCB-30 showed series agglomeration. In this case, rapid recombination of the partial photocarriers may have occurred in Cu₂O, limiting the photocatalytic activity. In addition, as the aforementioned XRD results, rCB-20 has lower crystallinity compared with rCB-10, but it showed higher photocatalytic activity, indicating that crystallinity is not the key factors in photocatalytic reaction among these samples.

Furthermore, it can be seen from Fig. 7a and b that the control experiments performed under various conditions exclude the possibility of chemical reduction of Cr(VI) and confirm the role of light and catalysts, also reveal the different effectiveness of various catalysts such as rGO/Cu₂O, rGO/BiOBr, Cu₂O/BiOBr, rGO and rCB-x etc. in the photocatalytic reduction of Cr(VI). Why does the rCB-20 catalyst have high catalytic activity will be discussed in detail later in the photocatalysis mechanism section.

It should be pointed out that according to the aforementioned XPS results, a little zero-valent Bismuth was formed in the preparation process of rCB-20 sample. Whereas the Bi 4f XPS spectrum of the Cu₂O/BiOBr sample also exhibits the existence of the zero-valent bismuth (Fig. S4). But the rCB-20 sample presents a higher photocatalytic activity than that of the Cu₂O/BiOBr sample, indicating that it is rGO rather than metallic Bi accelerats the electron transport [70,71].

Fig. 7c shows the concentration variation of total chromium and Cr(VI) in the solution during photoreduction in the presence of the rCB-20

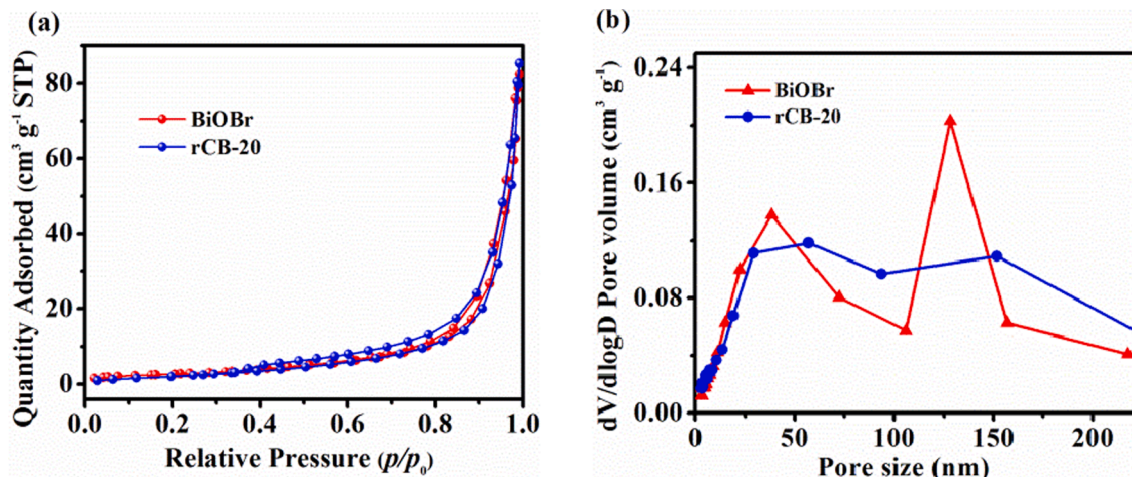


Fig. 6. (a) Nitrogen adsorption-desorption isotherms and (b) pore size distribution curves of the BiOBr and rCB-20 samples.

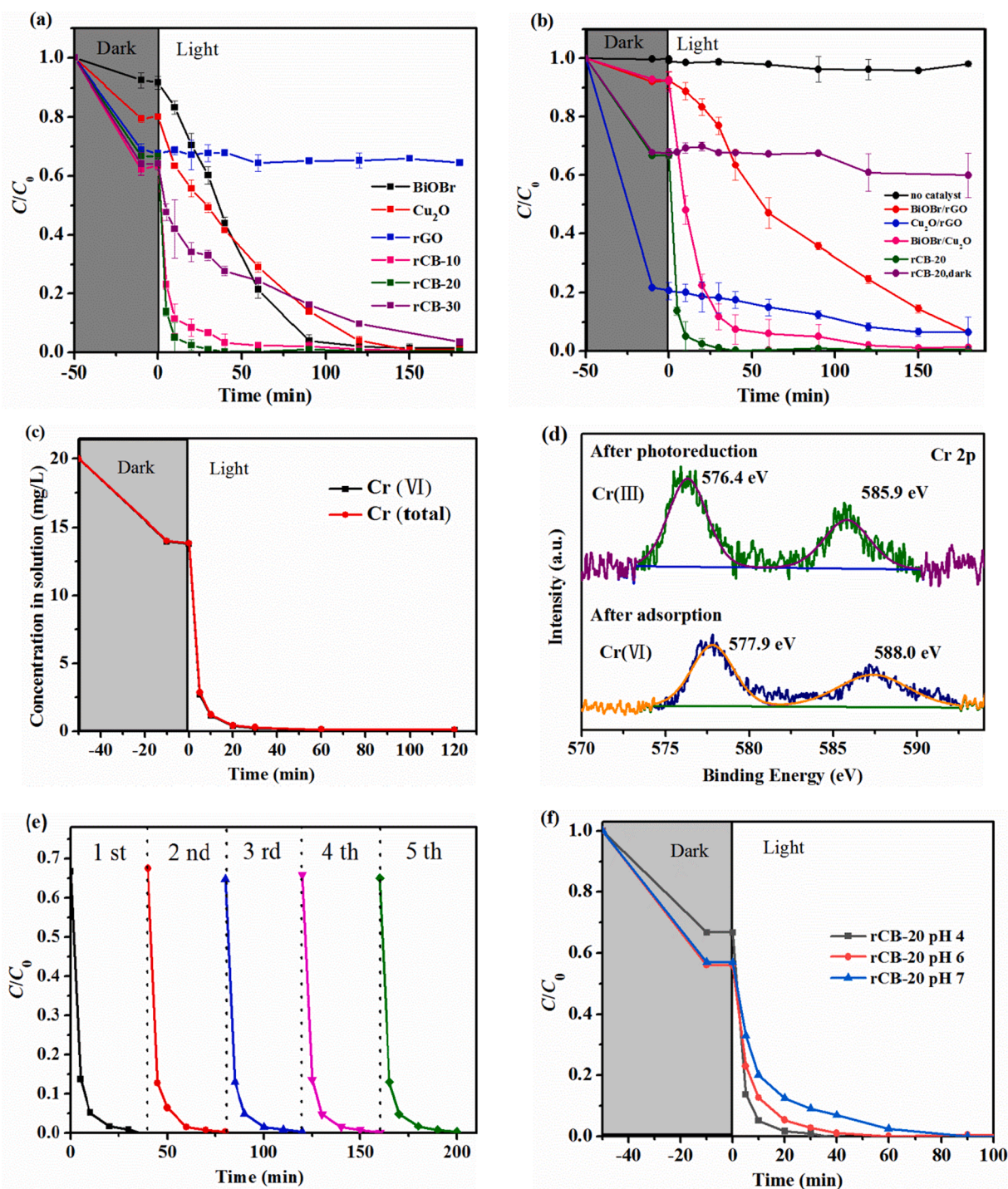


Fig. 7. (a), (b) The dark adsorption and photoreduction of Cr(VI) in the presence of different catalysts; (c) the concentration variation of the total chromium and Cr(VI) during photoreduction in the presence of the rCB-20 catalyst; (d) high-resolution XPS spectra of Cr 2p before and after photocatalytic reaction; (e) the reuse stability of the rCB-20 photocatalyst in the reduction of Cr(VI). The initial Cr(VI) concentration = $20 \text{ mg}\cdot\text{L}^{-1}$; catalyst dosage = 20 mg ; pH = 4; (f) The dark adsorption and photoreduction of Cr(VI) in the presence of the rCB-20 photocatalyst at different pH.

catalyst. It can be seen that the concentration change curves of the total chromium and Cr(VI) are almost overlapped. Meanwhile, no Cr(III) was detected in the solution. These results suggest that the Cr(III) generated by the photoreduction of Cr(VI) was completely adsorbed on the surface of the rCB-20 catalyst. The high resolution XPS spectra of the Cr 2p in Fig. 7d also prove this point. It can be seen that after adsorption of Cr(VI) the rCB-20 sample presents two peaks appearing at 577.9 and 588.0 eV, which are attributed to the characteristic peaks of Cr(VI) [55]; however, after photocatalytic reduction of Cr(VI) the rCB-20 catalyst also exhibits

two peaks, but arise at 576.4 and 585.9 eV, which are assigned to Cr(III) [55]. Therefore, the phenomenon of that the Cr(III) generated through the photocatalytic reduction of Cr(VI) can be completely adsorbed on the surface of the rCB-20 indicates that using rCB-20 as photocatalyst can effectively remove chromium in the solution.

In addition to catalytic activity, stability is also an important parameter to measure the performance of catalysts. Because of this, the reuse tests of the rCB-20 catalyst in the photocatalytic reduction of Cr(VI) were performed. The results are shown in Fig. 7e. It can be seen that

the photocatalytic activity of the rCB-20 catalyst is almost not lost after reuse of five cycles, showing a good stability in activity. Whereas the XRD characterization certify the structural stability of the rCB-20 catalyst. As shown in Fig. S5, the XRD pattern of the rCB-20 catalyst is nearly unchanged after used to the photocatalytic reduction of Cr(VI). Therefore, the rCB-20 catalyst is stable in structure. In order to further evidence this point, the Cu 2p XPS spectra of the rCB-20 catalyst were measured after it suffered from photocatalytic reaction. The results are illustrated in Fig. S6. revealed two main peaks: $2p_{3/2}$ at 932.15 eV and $2p_{1/2}$ at 951.84 eV (Fig. S6a), corresponding to Cu^+ [67,68]. Whereas, for pure Cu_2O (shown in Fig. S6b), the peaks of Cu^+ were decreased after the photocatalytic reaction. Meanwhile, the peaks at 933.6, 940.9, 943.4, and 953.7 eV, which correspond to the higher valence state of Cu [67,68] were increased. This suggests that pure Cu_2O is not stable in the photocatalytic process and the photocorrosion of Cu_2O can be suppressed in rCB-20. In addition, the effect of solution pH cannot also be ignored because Cr(VI) is a strong oxidant in acidic solutions [41]. Moreover, the wastewater containing Cr(VI) is harsh to be treated under acidic conditions. As shown in Fig. 7f, when the solution acidity changes in the pH range of 4 to 6, the photocatalytic reduction of Cr(VI) at pH = 4 gives the best effectiveness. More than 4 of pH, the less acidic, the less effective. However, a complete removal of Cr(VI) is still obtained within 90 min at pH = 7. In fact, Cr(VI) will react with Cu_2O when the pH of the solution is less than 4, resulting in the oxidation of Cu(I).

3.3. Photocatalysis mechanism

As mentioned above, the rCB-20 composite catalyst has a very high photocatalytic activity for photoreduction of Cr(VI). This can be explained by its rough surface with a mastoid morphology and its reasonable band gap structure. The former can reduce light reflection, in favor of light absorption; and the latter can facilitate the separation of photogenerated carriers and reduce the recombination of photoelectrons and holes. In order to account for the effect caused by changes in band gap structure due to the composite of BiOBr with Cu_2O , The photoluminescence (PL) spectra of the pristine BiOBr and rCB-20 samples were measured using a photoluminescence spectrometer. The results are presented in Fig. 8a. It can be seen that the fluorescence emission intensity of the rCB-20 is much lower than that of the pristine BiOBr. Generally, high PL emission intensity implies a high recombination rate of photogenerated electrons and holes [53]. Obviously, compared to the pristine BiOBr, the rCB-20 composite has a band gap structure that is more favorable for photogenerated carrier separation. Even so, the resistance of carrier migration also affects the separation efficiency of electron-hole pair. Thus, EIS measurements were performed to investigate the resistance of charge transfer in the materials.

In general, the arc radius of the Nyquist plot in EIS is proportional to the interface electron transfer resistance [70]. As can be seen from Fig. 8b, the rCB-20 composite shows the smallest arc radius compared to those of the Cu_2O , BiOBr and $\text{Cu}_2\text{O}/\text{BiOBr}$, indicating that the rCB-20 composite has the least interfacial charge transfer resistance. This is related to the combination of Cu_2O and BiOBr on one hand, and the existence of rGO on the other hand. The interface double electrical layer (heterojunction) formed owing to the combination of Cu_2O and BiOBr can drive the charge migration; whereas the existence of rGO can reduce the resistance of electron transfer due to its very high conductivity (as illustrated in Scheme S1).

The formation of interfacial double layer (heterojunction) plays an important role in charge transfer in semiconductors. This means that an electric field (E) is established in the space charge region near the interface inside the composite material. The direction of electric field can be determined by using KPFM. The results of KPFM measurement is presented in Fig. 9. Thereinto, Fig. 9a is an intuitive image of the surface photovoltage distribution of the rCB-20 composite under dark, and Fig. 9b under visible light irradiation ($\lambda > 400$ nm); whereas Fig. 9c shows the corresponding surface potential from location A to B in the intuitive image. It can be seen from Fig. 9c that after suffered from visible light irradiation the surface potential of location A (Cu_2O) decreased by approximately 8 mV, whereas location B (BiOBr) increased by approximately 10 mV. This result demonstrates that the direction of the electric field is from Cu_2O to BiOBr, consistent with the result of XPS characterization. Therefore, the photogenerated electrons would transfer from BiOBr to Cu_2O under visible light irradiation. Whereas the rGO acts as an electronic medium to improve electric conductivity [70,71].

Based on the above experimental results, a schematic diagram concerning photocatalysis mechanism is proposed and illustrated in Fig. 10. According to the mechanism diagram, the photocatalytic principle of the rCB-20 composite catalyst can be clearly elucidated. Upon light irradiation, electrons in the valence bands of Cu_2O and BiOBr are simultaneously photoexcited and transition to the conduction band, producing photoelectrons and holes. The photoelectrons in the BiOBr CB would transfer spontaneously into the VB of Cu_2O due to the driven role of self-built electric field, making the charge of the photogenerated holes in the Cu_2O VB be compensated. The electrons in the Cu_2O CB migrate to the surface through the medium role of rGO and are captured by Cr(VI), leading to the reduction of Cr(VI). Whereas the hole charge in the VB of BiOBr is compensated by the oxidation of water molecules in the solution. Such a photocatalytic process is called as “Z-scheme” mechanism, and the rCB-20 composite as “Z-scheme” heterojunction photocatalyst.

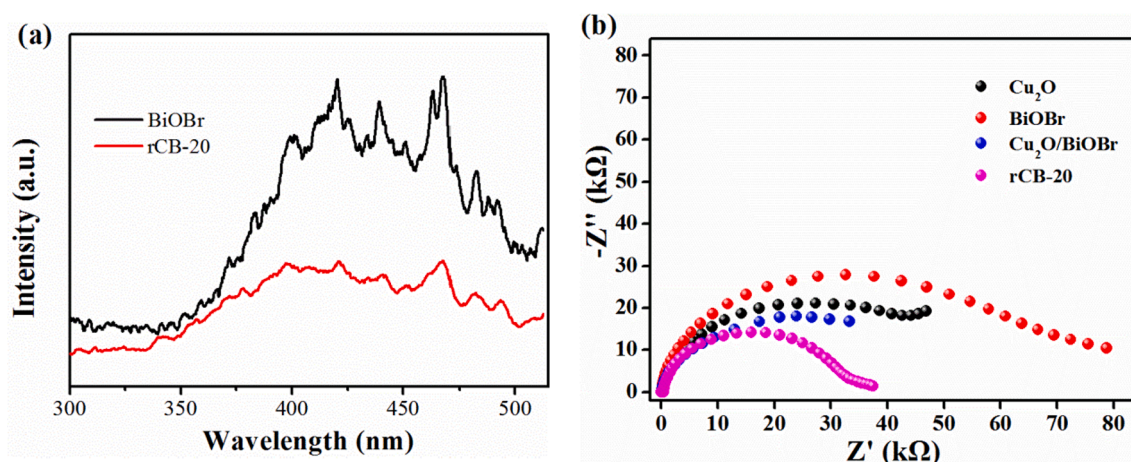


Fig. 8. (a) Photoluminescence spectra of the BiOBr and rCB-20 samples. (b) EIS of the Cu_2O , BiOBr, $\text{Cu}_2\text{O}/\text{BiOBr}$ and rCB-20 samples.

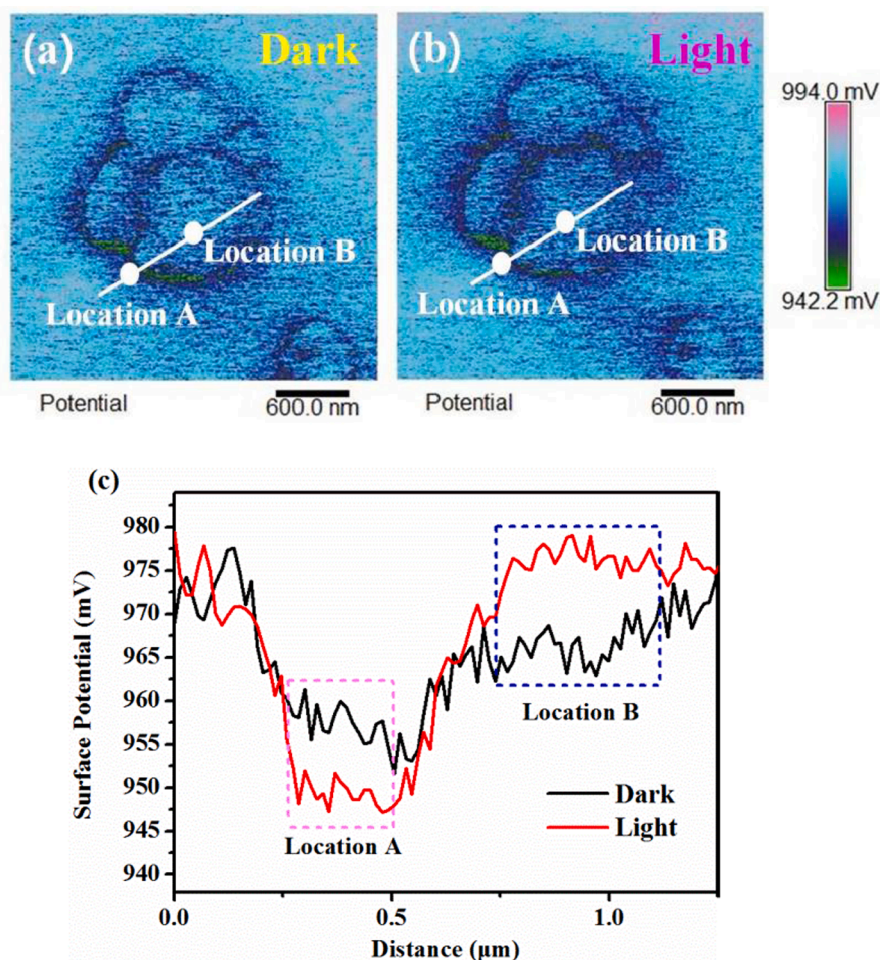


Fig. 9. Surface photovoltage distribution of rCB-20 in the dark (a) and visible light irradiation (b). (c) Surface photovoltage of rCB-20 under dark and visible light irradiation.

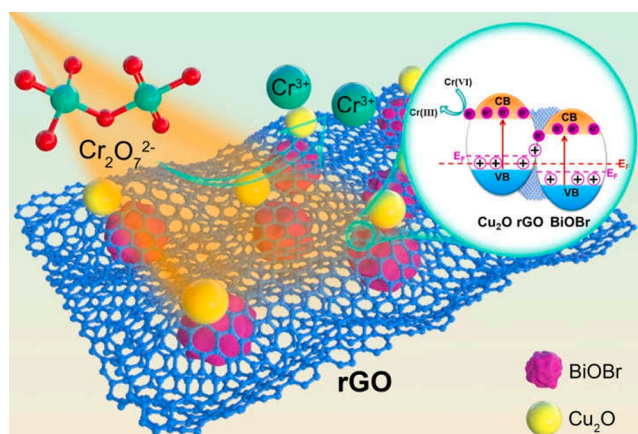


Fig. 10. Schematic diagram of the photocatalysis mechanism of the rCB composite catalyst.

4. Conclusions

A series of Cu₂O/rGO/BiOBr “Z-scheme” composite materials (rCBs) were prepared. They displayed much better photocatalytic performance than the individual Cu₂O or BiOBr for reducing Cr(VI) in an acid solution under visible light irradiation, and the optimal amount of Cu₂O was 20% (rCB-20). Even in a neutral media, the rCB-20 photocatalyst can also

completely remove Cr(VI) within 90 min. Suitable band structure matching between Cu₂O and BiOBr and formation of Z-scheme heterojunction favor the transfer and separation of photogenerated carriers, and meanwhile favor enhancing the redox capacity of photocatalyst. This work provides a facile and feasible approach to construct new visible-light-responsive photocatalysts.

CRediT authorship contribution statement

Jian Ma: Data curation, Funding acquisition, Writing - original draft. **Congjie Liang:** Data curation, Formal analysis, Investigation. **Changjiang Yu:** Investigation, Validation. **Huaming Li:** Formal analysis. **Hui Xu:** Validation. **Yingjie Hua:** Project administration, Supervision, Methodology, Resources. **Chongtai Wang:** Conceptualization, Methodology, Supervision, Writing - review & editing.

Declaration of Competing Interest

The authors declare that they have no known competing financial interests or personal relationships that could have appeared to influence the work reported in this paper.

Data availability

Data will be made available on request.

Acknowledgments

This work was supported by Hainan Provincial Natural Science Foundation of China (2019RC180), and Key Research and Development Project of Hainan Province of China (ZDYF2020079).

Appendix A. Supplementary data

Supplementary data to this article can be found online at <https://doi.org/10.1016/j.apsusc.2022.155247>.

References

- [1] Z.A. Zakaria, W.A. Ahmad, Cr(VI) removal using the combination of the Cr(VI)-resistant and Cr(VI)-reducing biofilm and the alum-polyacrylamide, *Water Air Soil Pollut.* 231 (10) (2020) 490.
- [2] Y. Wen, Z. Huang, M. Zhao, L.S. Zhao, Enhanced visible-light-driven photocatalytic activity of bi-phase titanium dioxide@covalent organic framework Z-scheme system for photocatalytic removal of Cr(VI), *Appl. Surf. Sci.* 596 (2022), 153485.
- [3] K.Z. Elwakeel, A.M. Elgarayh, Z.A. Khan, M.S. Almughamisi, A.S. Al-Bogami, Perspectives regarding metal/mineral-incorporating materials for water purification: with special focus on Cr(VI) removal, *Mater. Adv.* 1 (2020) 1546–1574.
- [4] X.Q. Wang, W.X. Liu, J. Tian, Z.H. Zhao, P. Hao, X.L. Kang, Y.H. Sang, H. Li, Cr(VI), Pb(II), Cd(II) adsorption properties of nanostructured BiOBr microspheres and their application in a continuous filtering removal device for heavy metal ions, *J. Mater. Chem. A* (2014) 2599.
- [5] G. Li, F. Qin, H. Yang, Z. Lu, H. Sun, R. Chen, Facile microwave synthesis of 3D flowerlike BiOBr nanostructures and their excellent Cr(VI) removal capacity, *Eur. J. Inorg. Chem.* 15 (2012) 2508–2513.
- [6] X. Li, D. Chen, N. Li, Q. Xu, H. Li, J. He, J. Lu, Efficient reduction of Cr(VI) by a BMO/Bi₂S₃ heterojunction via synergistic adsorption and photocatalysis under visible light, *J. Hazard. Mater.* 400 (2020), 123243.
- [7] L. Jia, W. Zhou, X. Huang, Y. Zhang, Q. Zhang, X. Tan, T. Yu, Enhanced adsorption of Cr(VI) on BiOBr under alkaline conditions: Interlayer anion exchange, *Environ. Sci.: Nano.* 6 (2019) 3601–3610.
- [8] A. Sharma, H. Lee, B. Ahn, Tailoring compressive strength and absorption energy of lightweight multi-phase AlCuSiFeX (X = Cr, Mn, Zn, Sn) high-entropy alloys processed via powder metallurgy, *Materials* 14 (17) (2021) 4945.
- [9] S. Zhao, Z. Chen, J. Shen, Y. Qu, B. Wang, X. Wang, Enhanced Cr(VI) removal based on reduction-coagulation-precipitation by NaBH₄ combined with fly ash leachate as a catalyst, *Chem. Eng. J.* 322 (2017) 646–656.
- [10] B. Xie, C. Shan, Z. Xu, X. Li, X. Zhang, J. Chen, B. Pan, One-step removal of Cr(VI) at alkaline pH by UV/sulfite process: Reduction to Cr(III) and in situ Cr(III) precipitation, *Chem. Eng. J.* 308 (2017) 791–797.
- [11] I. Benisti, Y. Paz, Transient FTIR measurements at nanoseconds resolution: correlating between faceting and photocatalytic activity in BiOCl, *J. Electrochem. Soc.* 166 (5) (2019) 3257–3264.
- [12] T. Li, Y. Gao, L. Zhang, X. Xing, X. Huang, F. Li, Y. Jin, C. Hu, Enhanced Cr(VI) reduction by direct transfer of photo-generated electrons to Cr 3d orbitals in CrO₄²⁻-intercalated BiOBr with exposed (110) facets, *Appl. Catal. B Environ.* 277 (2020), 119065.
- [13] Y. Shi, X. Xiong, S. Ding, X. Liu, Q. Jiang, J. Hu, In-situ topotactic synthesis and photocatalytic activity of plate-like BiOCl/2D networks Bi₂S₃ heterostructures, *Appl. Catal. B Environ.* 220 (2018) 570–580.
- [14] H. Wang, S. Chen, D. Yong, X. Zhang, S. Li, W. Shao, X. Sun, B. Pan, Y. Xie, Giant electron-hole interactions in confined layered structures for molecular oxygen activation, *J. Am. Chem. Soc.* 139 (13) (2017) 4737–4742.
- [15] K. Wang, Z. Qian, W. Guo, Multi-heterojunction of SnO₂/Bi₂O₃/BiOI nanofibers: Facile fabrication with enhanced visible-light photocatalytic performance, *Mater. Res. Bull.* 111 (2019) 202–211.
- [16] S. Wang, C. Yao, Y. Cai, Y. Yang, H. Ma, B.J. Jiang, J. Ma, Construct α-Fe₂O₃/rGO/PS composite structure for promoted spatial charge separation and exceptional catalytic activity in visible-light-driven photocatalysis-persulfate activation coupling system, *J. Alloy. Compd.* 898 (2022), 162829.
- [17] Y. Wang, S. Chen, D. Jin, A. Gong, X. Xu, C. Wu, Facile one-step solvothermal synthesis of active carbon/BiOI microspheres with enhanced visible light-driven photocatalytic activity in the reduction of Cr(VI), *RSC Adv.* 8 (14) (2018) 7518–7522.
- [18] M. Li, R. Ramachandran, T. Sakthivel, F. Wang, Z.-X. Xu, Siloxene: an advanced metal-free catalyst for efficient photocatalytic reduction of aqueous Cr(VI) under visible light, *Chem. Eng. J.* 421 (2021), 129728.
- [19] Y.-X. Li, H. Fu, P. Wang, C. Zhao, W. Liu, C.-C. Wang, Porous tube-like ZnS derived from rod-like ZIF-L for photocatalytic Cr(VI) reduction and organic pollutants degradation, *Environ. Pollut.* 256 (2020), 113417.
- [20] S. Zhang, Y. Zhao, R. Shi, C. Zhou, T. Zhang, Sub-3 nm Ultrafine Cu₂O for visible light driven nitrogen fixation[J], *Angew. Chem.* 60 (5) (2020) 2554–2560.
- [21] B. Qin, Y. Zhao, H. Li, L. Qiu, Z. Fan, Facet-dependent performance of Cu₂O nanocrystal for photocatalytic reduction of Cr(VI), *Chinese J. Catal.* 36 (8) (2015) 1321–1325.
- [22] C. Liu, X. Cui, Y. Li, Q. Duan, A hybrid hollow spheres Cu₂O@TiO₂-g-ZnTAPc with spatially separated structure as an efficient and energy-saving day-night photocatalyst for Cr(VI) reduction and organic pollutants removal, *Chem. Eng. J.* 399 (2020), 125807.
- [23] C.H. Cao, L. Xiao, C.H. Chen, Q.H. Cao, Synthesis of novel Cu₂O/BiOCl heterojunction nanocomposites and their enhanced photocatalytic activity under visible light, *Appl. Surf. Sci.* 357 (2015) 1171–1179.
- [24] W.D. Bai, M.B. Wu, X.L. Du, W.L. Gong, Y.H. Ding, C.H. Song, L. Liu, Synergistic effect of multiple-phase rGO/CuO/Cu₂O heterostructures for boosting photocatalytic activity and durability, *Appl. Surf. Sci.* 544 (2021), 148607.
- [25] B.A. Marinho, R.O. Cristóvão, J.M. Loureiro, R.A.R. Boaventura, V.J.P. Vilar, Solar photocatalytic reduction of Cr(VI) over Fe(III) in the presence of organic sacrificial agents, *Appl. Catal. B Environ.* 192 (2016) 208–219.
- [26] K. Li, Y. Liang, J. Yang, H. Zhang, G. Yang, W. Lei, BiOCl/Fe₂O₃ heterojunction nanoplates with enhanced visible-light-driven photocatalytic performance for degrading organic pollutants and reducing Cr(VI), *J. Photoch. Photobio. A* 364 (2018) 240–249.
- [27] Y. Liang, W. Xu, J. Fang, Z. Liu, D. Chen, T. Pan, Y. Yu, Z. Fang, Highly dispersed bismuth oxide quantum dots/graphite carbon nitride nanosheets heterojunctions for visible light photocatalytic redox degradation of environmental pollutants, *Appl. Catal. B Environ.* 295 (2021), 120279.
- [28] Z. Liu, Q. Wang, X. Tan, Y. Wang, R. Jin, S. Gao, Enhanced photocatalytic performance of TiO₂ NTs decorated with chrysanthemum-like BiOI nanoflowers, *Sep. Purif. Technol.* 215 (2019) 565–572.
- [29] S. Asadzadeh-Khaneghah, A. Habibi-Yangjeh, K. Yubuta, Novel g-C₃N₄ nanosheets/CDs/BiOCl photocatalysts with exceptional activity under visible light, *J. Am. Ceram. Soc.* 102 (3) (2019) 1435–1453.
- [30] Y. Li, B. Wang, S. Liu, X. Duan, Z. Hu, Synthesis and characterization of Cu₂O/TiO₂ photocatalysts for H₂ evolution from aqueous solution with different scavengers, *Appl. Surf. Sci.* 324 (2015) 736–744.
- [31] W.J. Li, G.S. Zhou, X.D. Zhu, M.S. Song, P.P. Wang, C.C. Ma, X.L. Liu, S. Han, Y. Q. Huang, Z.Y. Lu, Magnetic assembly synthesis of high-efficiency recyclable flower-like MoS₂@Fe₃O₄@Cu₂O like Z-scheme heterojunction towards efficient photodegradation of tetracycline, *Appl. Surf. Sci.* 555 (2021), 149730.
- [32] M.E. Malefane, P.J. Mafa, T.T.I. Nkambule, M.E. Managa, A.T. Kuvarega, Modulation of Z-scheme photocatalysts for pharmaceuticals remediation and pathogen inactivation: Design Devotion, Concept Examination, and Developments, *Chem. Eng. J.* 452 (2023) 138894, <https://doi.org/10.1016/j.cej.2022.138894>.
- [33] M.E. Malefane, U. Feleni, A.T. Kuvarega, Cobalt (II/III) oxide and tungsten (VI) oxide p-n heterojunction photocatalyst for photodegradation of diclofenac sodium under visible light, *J. Environ. Chem. Eng.* 8 (2020), 103560.
- [34] S.J.A. Moniz, S.A. Shevlin, D.J. Martin, Z.X. Guo, J.W. Tang, Visible-light driven heterojunction photocatalysts for water splitting – a critical review, *Energy Environ. Sci.* 731 (2015).
- [35] M.E. Malefane, U. Feleni, P.J. Mafa, A.T. Kuvarega, Fabrication of direct Z-scheme Co₃O₄/BZIOI for ibuprofen and trimethoprim degradation under visible light irradiation, *Appl. Surf. Sci.* 514 (2020), 145940.
- [36] G. Li, F. Qin, R. Wang, S. Xiao, H. Sun, R. Chen, BiOX (X=Cl, Br, I) nanostructures: Mannitol-mediated microwave synthesis, visible light photocatalytic performance, and Cr(VI) removal capacity, *J. Colloid. Interf. Sci.* 409 (2013) 43–51.
- [37] H. Li, L. Zhang, Oxygen vacancy induced selective silver deposition on the 001 facets of BiOCl single-crystalline nanosheets for enhanced Cr(VI) and sodium pentachlorophenate removal under visible light, *Nanoscale* 6 (14) (2014) 7805–7810.
- [38] Z. Wu, Z. Li, Q. Tian, J. Liu, S. Zhang, K. Xu, J. Shen, S. Zhang, W. Wu, Protonated Branched Polyethyleneimine Induces the Shape Evolution of BiOCl and Exposed {010} Facet of BiOCl Nanosheets, *Cryst. Growth Des.* 18 (9) (2018) 5479–5491.
- [39] J. Yang, Y. Liang, K. Li, G. Yang, Y. Zhu, S. Liu, W. Lei, New reaction pathway induced by the synergistic effects of Bi plasmon and La³⁺ doping for efficient visible light photocatalytic reaction on BiOCl, *Appl. Surf. Sci.* 458 (2018) 769–780.
- [40] J. Yang, Y.J. Liang, K. Li, G. Yang, S. Yin, One-step low-temperature synthesis of 0D CeO₂ quantum dots/2D BiOX (X = Cl, Br) nanoplates heterojunctions for highly boosting photo-oxidation and reduction ability, *Appl. Catal. B Environ.* 250 (2019) 17–30.
- [41] Z. Shi, Y. Zhang, G.M. Duorokun, W. Cao, T. Liu, L.S. Zhang, J.S. Liu, M.Q. Li, Z.G. Chen, Fabrication of MoS₂/BiOBr heterojunctions on carbon fibers as a weavable photocatalyst for tetracycline hydrochloride degradation and Cr(VI) reduction under visible light, *Environ. Sci.: Nano* (2020) 2708.
- [42] Z.Q. Long, G.M. Zhang, H.B. Du, J. Zhu, J.W. Li, Preparation and application of BiOBr-Bi₂S₃ heterojunctions for efficient photocatalytic removal of Cr(VI), *J. Hazard. Mater.* 407 (2021), 124394.
- [43] R. Jiang, H.Y. Zhu, J.B. Li, F.Q. Fu, J. Yao, S.T. Jiang, G.M. Zeng, Fabrication of novel magnetically separable BiOBr/CoFe₂O₄ microspheres and its application in the efficient removal of dye from aqueous phase by an environment-friendly and economical approach, *Appl. Surf. Sci.* 364 (2016) 604–612.
- [44] Y. Bao, K. Chen, Novel Z-scheme BiOBr/reduced graphene oxide/protonated g-C₃N₄ photocatalyst: synthesis, characterization, visible light photocatalytic activity and mechanism, *Appl. Surf. Sci.* 437 (2018) 51–61.
- [45] X. Li, L. Wang, L. Zhang, S. Zhuo, A facile route to the synthesis of magnetically separable BiOBr/NiFe₂O₄ composites with enhanced photocatalytic performance, *Appl. Surf. Sci.* 419 (2017) 586–594.
- [46] D. Hu, Y. Xu, S. Zhang, J. Tu, M. Li, L. Zhi, J. Liu, Fabrication of redox-mediator-free Z-scheme CdS/NiCo₂O₄ photocatalysts with enhanced visible-light driven photocatalytic activity in Cr(VI) reduction and antibiotics degradation, *Colloid. Surf. A* 608 (2021), 125582.
- [47] A. Kumar, G. Sharma, A. Kumari, C. Guo, M. Naushad, D.-V.-N. Vo, J. Iqbal, F. J. Stadler, Construction of dual Z-scheme g-C₃N₄/Bi₄Ti₃O₁₂/Bi₄O₅I₂ heterojunction for visible and solar powered coupled photocatalytic antibiotic degradation and

- hydrogen production: Boosting via I^-/I^{3-} and Bi^{3+}/Bi^{5+} redox mediators, *Appl. Catal. B Environ.* 284 (2021), 119808.
- [48] L. Wang, S. Karuturi, L. Zan, Bi_2S_3 - In_2S_3 Heterostructures for efficient photoreduction of highly toxic Cr^{6+} enabled by facet-coupling and Z-scheme structure, *Small* 17 (40) (2021) 2101833.
- [49] C. Zhou, S. Wang, Z. Zhao, Z. Shi, S. Yan, Z. Zou, A facet-dependent schottky-junction electron shuttle in a $BiVO_4\{010\}$ -Au- Cu_2O Z-scheme photocatalyst for efficient charge separation, *Adv. Funct. Mater.* 28 (31) (2018) 1801214.
- [50] F. Khan, M.S. Khan, S. Kamal, M. Arshad, S.I. Ahmad, S.A.A. Nami, Recent advances on Graphene oxide and reduced Graphene oxide based nanocomposites for photodegradation of dyes, *J. Mater. Chem. C* 8 (2020) 15940–15955.
- [51] A. Chen, Z. Bian, J. Xu, X. Xin, H. Wang, Simultaneous removal of $Cr(VI)$ and phenol contaminants using Z-scheme bismuth oxyiodide/reduced graphene oxide/bismuth sulfide system under visible-light irradiation, *Chemosphere* 188 (2017) 659–666.
- [52] W. Wang, Z. Wu, E. Eftekhari, Z. Huo, X. Li, M.O. Tade, C. Yan, Z. Yan, C. Li, Q. Li, D. Zhao, High performance heterojunction photocatalytic membranes formed by embedment of Cu_2O and TiO_2 nanowires in reduced Graphene oxide, *Catal. Sci. Technol.* 8 (2018) 1704–1711.
- [53] J. Ma, X. Tan, T. Yu, X. Li, Fabrication of g- C_3N_4 / TiO_2 hierarchical spheres with reactive $\{001\}$ TiO_2 crystal facets and its visible-light photocatalytic activity, *Int. J. Hydrogen Energ.* 41 (2016) 3877–3887.
- [54] Y. Li, H. Xu, S. Ouyang, D. Lu, X. Wang, D. Wang, J. Ye, In situ surface alkalinized g- C_3N_4 toward enhancement of photocatalytic H_2 evolution under visible-light irradiation, *J. Mater. Chem. A* 4 (2016) 2943–2950.
- [55] L.X. Jia, X. Tan, Y.F. Li, Y.Z. Zhang, S. Cao, W. Zhou, X. Huang, L.Q. Liu, T. Yu, Design of $BiOBr_{0.25}I_{0.75}$ for synergy photoreduction $Cr(VI)$ and capture $Cr(III)$ over wide pH range, *Chinese Chem. Lett.* 33 (2022) 3053–3060.
- [56] Y. Zhou, G. Liu, X. Zhu, Y. Guo, Cu_2O quantum dots modified by RGO nanosheets for ultrasensitive and selective NO_2 gas detection, *Ceram. Int.* 43 (11) (2017) 8372–8377.
- [57] Y. Pu, H.Y. Chou, W.S. Kuo, K.H. Wei, Y.J. Hsu, Interfacial charge carrier dynamics of cuprous oxide-reduced graphene oxide (Cu_2O -rGO) nanoheterostructures and their related visible-light-driven photocatalysis, *Appl. Catal. B Environ.* 204 (2017) 21–32.
- [58] Z. Fan, Y. Zhao, W. Zhai, L. Qiu, H. Li, M.R. Hoffmann, Facet-dependent performance of $BiOBr$ for photocatalytic reduction of $Cr(VI)$, *RSC Adv.* 6 (3) (2016) 2028–2031.
- [59] R. Yang, X. Lu, X. Huang, Z. Chen, X. Zhang, M. Xu, Q. Song, L. Zhu, Bi-component Cu_2O - $CuCl$ composites with tunable oxygen vacancies and enhanced photocatalytic properties, *Appl. Catal. B Environ.* 170–171 (2015) 225–232.
- [60] W. Cui, W. An, L. Liu, J. Hu, Y. Liang, Novel Cu_2O quantum dots coupled flower-like $BiOBr$ for enhanced photocatalytic degradation of organic contaminant, *J. Hazard. Mater.* 280 (2014) 417–427.
- [61] J. Han, G. Zhu, M. Hojamberdiev, J. Peng, X. Zhang, Y. Liu, B. Ge, P. Liu, Rapid adsorption and photocatalytic activity for Rhodamine B and $Cr(VI)$ by ultrathin $BiOI$ nanosheets with highly exposed 001 facets, *New J. Chem.* 39 (3) (2015) 1874–1882.
- [62] T. Li, G. Zhang, H. Lan, H. Liu, J. Qu, Enhanced photoreduction of chromium(VI) intercalated ion exchange in $BiOBr_{0.75}I_{0.25}$ layers structure by bulk charge transfer, *ACS Sustain. Chem. Eng.* 7 (2) (2018) 2429–2436.
- [63] Y. Dai, C. Li, Y. Shen, S. Zhu, M.S. Hvid, L.-C. Wu, J. Skibsted, Y. Li, J.W. H. Niemantsverdriet, F. Besenbacher, N. Lock, R. Su, Efficient solar-driven hydrogen transfer by bismuth-based photocatalyst with engineered basic sites, *J. Am. Chem. Soc.* 140 (48) (2018) 16711–16719.
- [64] J. Shang, W. Hao, X. Lv, T. Wang, X. Wang, Y. Du, S. Dou, T. Xie, D. Wang, J. Wang, Bismuth oxybromide with reasonable photocatalytic reduction activity under visible light, *ACS Catal.* 4 (3) (2014) 954–961.
- [65] H. Wang, D. Yong, S. Chen, S. Jiang, X. Zhang, W. Shao, Q. Zhang, W. Yan, B. Pan, Y. Xie, Oxygen-vacancy-mediated exciton dissociation in $BiOBr$ for boosting charge-carrier-involved molecular oxygen activation, *J. Am. Chem. Soc.* 140 (5) (2018) 1760–1766.
- [66] Q. Yu, J. Chen, Y. Li, M. Wen, H. Liu, G. Li, T. An, In-situ decoration of metallic Bi on $BiOBr$ with exposed (110) facets and surface oxygen vacancy for enhanced solar light photocatalytic degradation of gaseous n-hexane, *Chinese J. Catal.* 41 (10) (2020) 1603–1612.
- [67] L. Liu, X. Gu, C. Sun, H. Li, Y. Deng, F. Gao, L. Dong, In situ loading of ultra-small Cu_2O particles on TiO_2 nanosheets to enhance the visible-light photoactivity, *Nanoscale* 4 (20) (2012) 6351–6359.
- [68] U. Rajaji, S.V. Selvi, S.M. Chen, S. Chinnapaiyan, T.W. Chen, M. Govindasamy, A nanocomposite consisting of cuprous oxide supported on graphitic carbon nitride nanosheets for non-enzymatic electrochemical sensing of 8-hydroxy-2'-deoxyguanosine, *Microchim. Acta* 187 (8) (2020) 459.
- [69] W. Jo, T.S. Natarajan, Influence of TiO_2 morphology on the photocatalytic efficiency of direct Z-scheme g- C_3N_4 / TiO_2 photocatalysts for isoniazid degradation, *Chem. Eng. J.* 281 (2015) 549–565.
- [70] H. Li, F. Deng, Y. Zheng, L. Hua, C.H. Qu, X.B. Luo, Visible light driven Z-scheme rGO/ Bi_2S_3 - $BiOBr$ heterojunctions with tunable exposed $BiOBr$ (102) facets for efficient synchronous photocatalytic degradation of 2-nitrophenol and $Cr(VI)$ reduction, *Environ. Sci.: Nano* (2019) 3670.
- [71] X. Tang, X.L. Guo, Z.T. Chen, Y.Y. Liu, W.J. Zhang, Y.X. Wang, Y.M. Zheng, M. Zhang, Z.B. Peng, R. Li, Y.H. Zhao, Facile preparation of Cu_2O nanoparticles/ Bi_2WO_6 /rGO hybrid with enhanced photoelectrochemical performance, *Appl. Surf. Sci.* 510 (2020), 145447.